ADVANCED FUNCTIONAL MATERIALS
www.afm-journal.de

Assessment of Novel Long-Lasting Ceria-Stabilized Zirconia-Based Ceramics with Different Surface Topographies as Implant Materials

Brigitte Altmann, Lamprini Karygianni, Ali Al-Ahmad, Frank Butz, Maria Bächle, Erik Adolfsson, Tobias Fürderer, Nicolas Courtois, Paola Palmero, Marie Follo, Jérôme Chevalier, Thorsten Steinberg, and Ralf Joachim Kohal*

The development of long-lasting zirconia-based ceramics for implants, which are not prone to hydrothermal aging, is not satisfactorily solved. Therefore, this study is conceived as an overall evaluation screening of novel ceria-stabilized zirconia–alumina–aluminate composite ceramics (ZA_8Sr_8-Ce11) with different surface topographies for use in clinical applications. Ceria-stabilized zirconia is chosen as the matrix for the composite material, due to its lower susceptibility to aging than yttria-stabilized zirconia (3Y-TZP). This assessment is carried out on three preclinical investigation levels, indicating an overall biocompatibility of ceria-stabilized zirconia-based ceramics, both in vitro and in vivo. Long-term attachment and mineralized extracellular matrix (ECM) deposition of primary osteoblasts are the most distinct on porous ZA_8Sr_8-Ce11$_p$ surfaces, while ECM attachment on 3Y-TZP and ZA_8Sr_8-Ce11 with compact surface texture is poor. In this regard, the animal study confirms the porous ZA_8Sr_8-Ce11$_p$ to be the most favorable material, showing the highest bone-to-implant contact values and implant stability post implantation in comparison with control groups. Moreover, the microbiological evaluation reveals no favoritism of biofilm formation on the porous ZA_8Sr_8-Ce11$_p$ when compared to a smooth control surface. Hence, together with the in vitro in vivo assessment analogy, the promising clinical potential of this novel ZA_8Sr_8-Ce11 as an implant material is demonstrated.

1. Introduction

The development process of a novel biomaterial is multileveled and requires comprehensive evaluation and safety assessments of the material's effects on target tissues and their cells to ensure successful clinical use and maximum patient benefit.

In implant dentistry, zirconia-based oral implants became of interest, not only due to their excellent mechanical properties, but also due to their superior aesthetics and biocompatibility characteristics in vitro[1] and in vivo.[1e,2] In particular, the high strength, greater than 1200 MPa,[3] exhibited by yttria-stabilized zirconia ceramics (Y-TZP) allows them to resist intermittent forces that arise during mastication.[3,4] Before its application in dentistry, zirconia was used as a material for femoral head balls used in hip replacements. In 2001/2002, numerous femoral head failures occurred in certain batches processed with a new type of furnace.[5]

Dr. B. Altmann, Dr. F. Butz, Dr. M. Bächle, Prof. R. J. Kohal
Department of Prosthetic Dentistry
Medical Center – University of Freiburg
Faculty of Medicine
University of Freiburg
Hugstetter Strasse 55, 79106 Freiburg, Germany
E-mail: brigitte.altmann@uniklinik-freiburg.de
Dr. B. Altmann
G.E.R.N. Tissue Replacement, Regeneration & Neogenesis
Department of Oral and Maxillofacial Surgery
Medical Center – University of Freiburg
Faculty of Medicine
University of Freiburg
Hugstetter Straße 55, 79106 Freiburg, Germany
Dr. L. Karygianni, Prof. A. Al-Ahmad
Department of Operative Dentistry and Periodontology
Medical Center – University of Freiburg
Faculty of Medicine
University of Freiburg
Hugstetter Strasse 55, 79106 Freiburg, Germany
Dr. L. Karygianni
Clinic for Preventive Dentistry
Periodontology and Cariology
Center of Dental Medicine University of Zurich
Plattenstr. 11, CH 8032 Zurich, Switzerland
Dr. E. Adolfsson
Swerea IVF AB
Argongatan 30, 43153 Mölndal, Sweden
T. Fürderer
MOESCHTER GROUP Holding GmbH & Co. KG
Hesslingsweg 65 67, 44309 Dortmund, Germany
N. Courtois
ANTHOGYR R&D
2237 avenue A. Lasquin, 74700 Sallanches, France
Prof. P. Palmero
Department of Applied Science and Technology
INSTM R.U. PoliTO, LINCE Lab
Politecnico di Torino
Corso Duca degli Abruzzi, 24, 10129 Torino, Italy

DOI: 10.1002/adfm.201702512

The evaluation of the failures leads to the conclusion that the low stability of those femoral heads was due to increased hydrothermal aging or low temperature degradation (LTD) associated with a change in the process. The tetragonal (t) to monoclinic (m) transformation specific for metastabilized zirconia is responsible for the LTD phenomenon. The underlying mechanism of LTD is that the surrounding humidity reacts with oxygen on the zirconia surface, leading to the production of OH^- ions. These ions penetrate into the interior by grain boundary diffusion and fill up oxygen vacancies. In the end, this leads to t–m transformation on the surface, which results in material uplift and crack initiation. Humidity now has the possibility to penetrate deeper into the material, resulting in a sustained effect regarding the process of t–m transformation. Due to this process, the material loses its stability and in the most severe cases, this may lead to implant fracture.[5,6] The challenge now is to produce zirconia ceramics which are not prone to the hydrothermal aging, but are able to transform from the tetragonal into the monoclinic phase for enhancing transformation toughening. These zirconia ceramics should also have the same biological properties as the Y-TZP ceramics.

Within the LONGLIFE European project, we designed and developed innovative zirconia-based composites, in which equiaxial α-Al_2O_3 and elongated $SrAl_{12}O_{19}$ phases are dispersed in a ceria-stabilized zirconia matrix. For a detailed description of this ceria-stabilized zirconia–alumina–aluminate composite, the reader may refer to two recent papers on the synthesis of the composite material[7] and on its specific features in terms of mechanical properties.[8] In brief, the composite reaches an unprecedent degree of microstructure refinement, thanks to a novel, patented[9] nanopowder engineering route, in which commercial zirconia powders were coated by inorganic precursors of the second phases, which crystallize on the zirconia particle surface under proper thermal treatment.[7] Thanks to this powder-coating strategy and a fine tuning of the amount of ceria inside the zirconia matrix, we were thus able to process ultrafine composite structures after sintering, which exhibited a combination of mechanical properties never obtained so far.[7] The material exhibits high biaxial bending strength (up to 1.1 GPa) and fracture toughness (>10 MPa$\sqrt{m}$). Moreover, in these composite ceramic, zirconia transformation precedes failure, leading to a significant degree of transformation-induced ductility and an exceptionally high Weibull modulus, in the range typically reported for metals. Being stabilized with cerium instead of yttrium, the material did not exhibit any sensitivity to LTD. The results thus demonstrated the high potential of using these new strong, tough, and stable zirconia-based composites in structural biomedical applications, for example, in implant dentistry. In this application, a careful and thorough in vitro and in vivo investigation is necessary, with a specific attention on cell, tissue, and microorganism interactions with the implant material.

With regard to the risk assessment in vitro, the vast majority of studies aiming at examining cell response to implant materials utilize cells of nonhuman origin, or cells that do not represent oral implant targets. Frequently used cells in these experimental studies include human osteosarcoma[10] and mouse myoblast cell lines,[11] human mesenchymal stem cells,[12] osteoblasts derived from rat bone marrow,[13] or primary rat osteoblasts.[14] Numerous investigations have demonstrated significant differences in cell reactions in response to different culture conditions, such as the use of hormones and growth factors, as well as biomaterial surface characteristics. These differences were most likely related to the cell source and phenotype responding to the given experimental conditions.[15]

Therefore, the objective of this study was to examine the influence of this newly developed implant material on specific cell functions of implant-relevant target cells, that is, primary human alveolar bone osteoblasts, and compare these results with respect to transferability, with a concomitant risk assessment in vivo using an established rat model followed by histological analyses and biomechanical stability tests.

A further important point that has to be taken in account is that the maintenance of implant materials in the human body is primarily threatened by multibacterial colonization, namely biofilms able to colonize various material surfaces and inducing persistent biofilm-related infections[16] such as peri-implantitis.[17] The incidence of peri-implant inflammation has recently increased and was reported to vary between 28% and 56%, particularly in patients with history of periodontitis.[18] Therefore, we included an examination of the interaction of microorganisms and material surface in our assessment of this newly developed zirconia-based ceria-stabilized oral implant material.

2. Results and Discussion

2.1. Surface Characterization

For the following material and biological evaluation methods, the materials have been grouped on the basis of their chemical composition and surface treatments as follows: i) presintered 3Y-TZP substrates coated with a) 3Y-TZP, b) the new composite ceramic ZA_8Sr_8-Ce11; ii) sintered 3Y-TZP substrates coated with porous ZA_8Sr_8-Ce11 (referred to as ZA_8Sr_8-$Ce11_p$; p = porous); iii) sandblasted titanium (referred to as Ti).

Dr. M. Follo
Department of Medicine I, Medical Center – University of Freiburg
Faculty of Medicine
University of Freiburg
Hugstetter Strasse 55, 79106 Freiburg, Germany
Prof. J. Chevalier
INSA-Lyon
MATEIS UMR CNRS 5510
Université de Lyon
Bât. Blaise Pascal 7, Av. Jean Capelle, 69621 Villeurbanne, France
Prof. T. Steinberg
Department of Oral Biotechnology
Center for Dental Medicine
Medical Center – University of Freiburg
Faculty of Medicine
University of Freiburg
Hugstetter Strasse 55, 79106 Freiburg, Germany

The comparison of the biological performance on the new ZA_8Sr_8-Ce11 ceramic with established 3Y-TZP within group i) allowed us thereby evaluating the impact of the chemical properties of the new ceramic composite versus an established zirconia-based material, since both surfaces were generated using the same technique and therefore were displaying similar topographical features. By comparing in vitro and in vivo data on chemically identical but structurally different ZA_8Sr_8-Ce11 surfaces, namely porous ZA_8Sr_8-$Ce11_p$ versus ZA_8Sr_8-Ce11, we further obtained information on the direct influence of surface topography on cell functions and integration into bone tissue. The inclusion of a titanium control group which represents an already clinically applied "state-of-the-art" implant surface helped us to estimate the quality of the later clinical performance of the new ceramic composite.

Since different surface treatments were applied to the zirconia materials, we first analyzed biomaterial surface topography by scanning electron microscopy (SEM) and white light interferometry (IFM). The SEM analysis revealed that the surfaces of the different implant groups can be clearly distinguished from each other with regard to surface structure (**Figure 1**). The only exceptions were 3Y-TZP and ZA_8Sr_8-Ce11, which displayed a similar compact and grainy surface texture due to the comparable coating process. Disks for the in vitro evaluation and implants destined for the animal study were both made from bulk 3Y-TZP and afterward coated in the presintered state either with a colloidal suspension of 3Y-TZP or the zirconia-based composite ceramic ZA_8Sr_8-Ce11, respectively. When the coatings were applied on the presintered substrate of 3Y-TZP, the homogeneous shrinkage of both, the substrate and the coating during sintering, allowed the coating to be densified and tightly linked to the substrate. A high magnification figure shows that the single particles of both coatings were well sintered, leaving no pores between the particles (Figure 1, lower row). Both test surfaces were homogeneous and smooth, without sharp edges or extruding peaks or deep sharp valleys. By contrast, when the coating of the ZA_8Sr_8-$Ce11_p$ composite material was applied on a sintered substrate of 3Y-TZP, the sintering shrinkage of the coating during the densification was restricted due to the already fully dense substrate. This contributed to the formation of a porous surface with apparently high interconnectivity of the pores compared to the surfaces obtained when the coating was applied on presintered substrates. The surface of the Ti control group was airborne particles abraded with BCP (a mixture of hydroxyapatite (HA) and beta-tricalcium phosphate (β-TCP)) and passivated in acid. The resulting rough surface displayed a flaky appearance with sharp edges and multimorphological depressions. The abrasive BCP particles used obviously created the irregular impressions/valleys. The valleys' extensions ranged from ≈1 to more than 20 µm and created a nonhomogenous surface. Upon examining surface topography parameters of the implant surfaces to be used for in vitro testing, the main roughness parameters S_a and S_q indicate that the zirconia-based surfaces had comparable rough surface properties, ranging from S_a = 0.187 µm and S_q = 0.243 µm for 3Y-TZP to S_a = 0.228 µm and S_q = 0.293 µm for ZA_8Sr_8-$Ce11_p$ (**Table 1**), whereas the Ti control group showed the highest roughness (Table 1, S_a = 1.46 µm and S_q = 1.87 µm). In terms of the developed interfacial area ratio (S_{dr} in %), which describes surface enlargement as compared to a totally flat reference area, 3Y-TZP and ZA_8Sr_8-Ce11 had the lowest value with S_{dr} = 1.7%, followed by the porous ZA_8Sr_8-$Ce11_p$ surface (S_{dr} = 3.18%) and Ti showing the highest surface enlargement (S_{dr} = 47.69%) (1). The higher surface enlargement of ZA_8Sr_8-$Ce11_p$ compared to the corresponding zirconia-based surfaces can be attributed to the high number of peaks per area (S_{ds}) since a high density

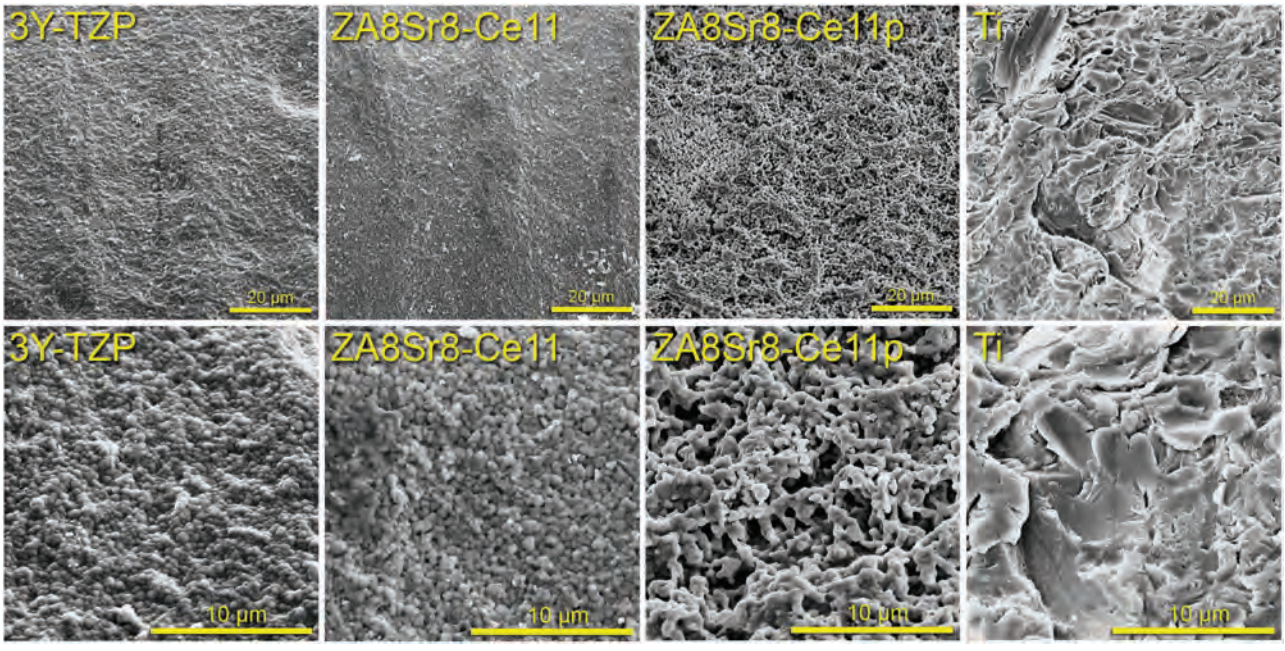

Figure 1. Scanning electron images of the implant test surfaces. SEM imaging parameters: extra high tension (EHT) voltage level = 12.00 kV; magnification = 1000× and 4000×.

Table 1. For 3D surface evaluation by interferometry, three disks and three miniature implants of each biomaterial surface were measured (mean values ± standard deviation (S.D.); n = 6–9). Surface parameters describing the topography of biomaterial surfaces were i) S_a (arithmetic mean of the absolute surface asperity departures from the reference datum), ii) S_q (root-mean-square value of asperity departures of a surface from the reference datum), iii) S_{dr} (surface enlargement compared to a totally flat reference area), and iv) S_{ds} (density of summits, i.e., number of peaks per area).

	Surface parameters			
	Average surface roughness (S_a) [µm] ± S.D.	Root-mean-square surface roughness (S_q) [µm] ± S.D.	Developed area ratio (S_{dr}) [%] ± S.D.	Summit density (S_{ds}) [pks mm^{-2}] ± S.D.
3Y-TZP	0.187 ± 0.021	0.243 ± 0.030	1.71 ± 0.09	95 971 ± 4698
ZA_8Sr_8-Ce11	0.211 ± 0.030	0.275 ± 0.035	1.70 ± 0.27	89 643 ± 6278
ZA_8Sr_8-Ce11$_p$	0.228 ± 0.009	0.293 ± 0.019	3.18[b] ± 0.66	103 723[b] ± 2526
Ti	1.455[a] ± 0.072	1.865[a] ± 0.081	47.69[a] ± 1.46	64 228[a] ± 1318
Impl. 3Y-TZP	0.319 ± 0.013	0.390 ± 0.016	3.29 ± 0.06	147 058 ± 2159
Impl.ZA_8Sr_8-Ce11	0.343 ± 0.027	0.416 ± 0.037	3.00 ± 0.13	148 142 ± 4774
Impl.ZA_8Sr_8-Ce11$_p$	0.773[b] ± 0.037	0.940[b] ± 0.043	43.00[b] ± 2.30	116 347[b] ± 2075
Imp.Ti	0.806[b] ± 0.083	1.090[a] ± 0.108	17.69[a] ± 2.40	82 766[a] ± 2650

[a]$p < 0.05$ significantly different from zirconia (3Y-TZP and ZA_8Sr_8-Ce11); [b]$p < 0.05$ significantly different from 3Y-TZP and ZA_8Sr_8-Ce11 (one way analysis of variance (ANOVA) followed by Tukey's post hoc test).

of peaks will contribute to surface enlargement. In summary, 3Y-TZP and ZA_8Sr_8-Ce11 demonstrated the smoothest surfaces, while the porous ZA_8Sr_8-Ce11$_p$ had a more pronounced surface roughness and Ti displayed the roughest surface properties.

With respect to the implant surfaces destined for the animal study (hereafter referred to as Impl.3Y-TZP, Impl.ZA_8Sr_8-Ce11, Impl.ZA_8Sr_8-Ce11$_p$, and Impl.Ti), the IFM data indicated moderate changes in the topography parameters S_a, S_q, and S_{dr} after transfer of the surface treatment process from 2D disks to 3D implants (Table 1). These modifications were characterized by a slight increase in all surface parameters of the zirconia-based materials, while simultaneously retaining the above-mentioned surface roughness trend within this group, namely similar surface properties for Impl.3Y-TZP (S_a = 0.32 µm; S_q = 0.39 µm; S_{dr} = 3.29%) and Impl.ZA_8Sr_8-Ce11 (S_a = 0.34 µm; S_q = 0.42; S_{dr} = 3.00%), and higher surface roughness of the porous Impl.ZA_8Sr_8-Ce11$_p$ surface (S_a = 0.773 µm; S_q = 0.94 µm; S_{dr} = 43.00%) (1). Therefore, Impl.3Y-TZP and Impl.ZA_8Sr_8-Ce11 could be classified as moderately rough surfaces and Impl.ZA_8Sr_8-Ce11$_p$ and Impl.Ti (S_a = 0.81 µm; S_q = 1.09 µm; S_{dr} = 17.69%) as rough surfaces.

2.2. Cell Culture Evaluation

Previous work on cell responses to differently structured implant surfaces revealed serious impacts of the surface topography on cell functions including primary cell adhesion, morphology, and proliferation.[19] Therefore, we first analyzed morphogenesis of osteoblasts on zirconia and titanium surfaces by SEM, fluorescence-based actin cytoskeleton staining, and quantitative morphometry after 1 and 7 d of culture (**Figure 2**).

Osteoblast morphology on zirconia surfaces differed considerably from titanium surfaces at day 1, as revealed by SEM (Figure 2A, upper row), thereby depicting differences in the surface structure of the implant materials. In detail, no morphological differences could be detected between osteoblasts grown on grainy or porous surface structures, with the cells showing similar spreading and a flattened morphology for all of the zirconia surfaces examined. However, on titanium surfaces, osteoblasts were less flattened compared to those grown on zirconia. They showed an elongated morphology with apparently limited contact at the surface grooves. A similar situation has been observed by fluorescence microscopy of phalloidin-labeled actin cytoskeleton in osteoblasts at day 1 on zirconia and titanium disks (Figure 2A, lower row). For zirconia-based surfaces, actin fluorescence appeared at the lateral and apical cell borders, indicating actin stress fibers due to tension sites at the lateral and apical cell margins, coinciding with cell adhesion by potential focal contacts. Conversely, on the rougher titanium surface, less actin bundling was observed, with strong actin fluorescence areas mainly located at the apical sites and throughout the cell soma, thereby suggesting that cell/surface contact was restricted to these areas. This is in agreement with observations from SEM, indicating that cell adhesion was apparently limited to the fractal surface protrusions of the titanium disks. Hence, the SEM analysis and actin cytoskeleton staining provide evidence for morphological differences of osteoblasts depending on surface topography of implant materials under study. To back up this suggestion, we performed fluorescence imaging software-based quantitative morphometric cell measurement at days 1 and 7 (Figure 2B and Table S1 (Supporting Information)) by determining the morphology index (the ratio between the long cell axis and short cell axis) describing the cell shape and the cell area, which in turn provides information about the degree of cell spreading. As already indicated in the qualitative microscopic analysis mentioned above, osteoblasts at day 1 discriminated between the different surface topographies, clearly showing the least elongated and spread morphology on the strongly structured titanium surface as represented by decreased morphology index and cell area as compared to cells on zirconia disks. This situation held true for osteoblasts at day 7 on titanium showing no changes in morphology index or cell area. Regarding morphogenesis

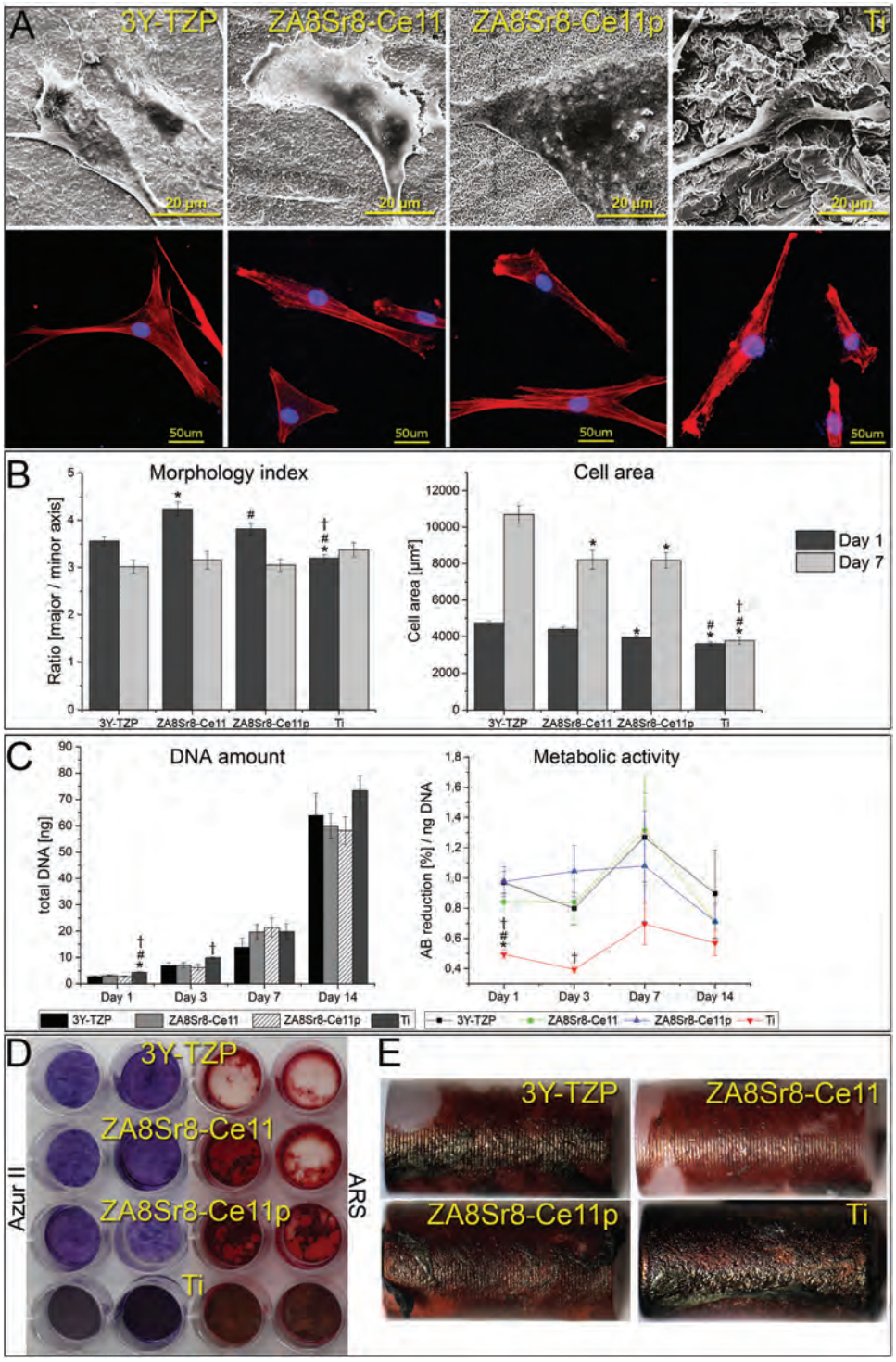

Figure 2. A) Scanning electron images (upper row) and actin cytoskeleton staining (lower row) of osteoblasts cultured for 24 h on 3Y-TZP, ZA_8Sr_8-Ce11, and titanium surfaces. B) Quantitative morphometric analysis of osteoblast morphology on zirconia and titanium surfaces at days 1 and 7 (mean ± standard error of the mean (S.E.M.); $n = 142–547$). C) Proliferation and metabolic activity of osteoblasts are represented by total DNA content in cell lysates and cellular reduction of the resazurin-based reporter dye alamarBlue (AB) at days 1, 3, 7, and 14 (mean ± S.E.M.; $n = 9$). D) Azur II and Alizarin Red S (ARS) staining of osteoblasts cultured for 28 d. Azur II (blue color) visualizes osteoblast monolayers under growth conditions, and ARS (red color) shows calcium deposition. E) ARS staining of osteoblasts cultured for 28 d on miniature implants. $^{*}p < 0.05$ significantly different from 3Y-TZP; $^{\#}p < 0.05$ significantly different from ZA_8Sr_8-Ce11; $^{\dagger}p < 0.05$ significantly different from ZA_8Sr_8-$Ce11_p$ (morphometry: Kruskal–Wallis ANOVA followed by Dunn's post hoc test; proliferation and AB: one way ANOVA followed by Tukey's post hoc test). SEM imaging parameters: EHT voltage level = 8.00 kV; magnification = 1000× and 4000×.

on zirconia surfaces, osteoblasts showed significant changes in cell morphology during continuous culture, as characterized by decreasing morphology index and expanding cell area from day 1 to day 7, thereby indicating that cells changed to a less elongated and more spread morphology at later culture time points. Osteoblasts on 3Y-TZP therefore displayed the most spread morphology, while cell spreading on both ZA_8Sr_8-Ce11 surfaces appeared to a lesser extent. These cell morphological differences between zirconia and titanium surfaces are in agreement with previous observations showing a more spread osteoblast morphology on smoother surfaces when compared with rougher and strongly structured surfaces.[19,20] Of particular interest is the fact that intersurface comparison between 3Y- and ZA_8Sr_8-Ce11 yielded different degrees of cell spreading irrespective of the surface topography, with a significantly less spread osteoblast morphology on both ZA_8Sr_8-Ce11 surfaces. This observation indicates that within the ceramic group, cell spreading was modulated by the biomaterial chemistry, rather than by surface topography.

SEM analysis and actin cytoskeleton staining provide evidence for morphological differences of osteoblasts depending on surface topography and chemistry. Therefore, we next examined putative surface-dependent effects on cell proliferation and mitochondrial activity. For this purpose, we determined the DNA concentration in cell lysates and the reduction of the resazurin-based reporter dye alamarBlue (AB) in mitochondria by employing the same osteoblast cultures for the analyzed time points, namely 1, 3, 7, and 14 d. Since DNA quantity correlates directly with cell number, DNA concentration in our samples provided information about the amount of adherent cells on the different implant materials, and allowing conclusions to be made about cell proliferation on the biomaterials under study. Subsequent normalization of the metabolic AB reduction on DNA quantity also enabled the evaluation of the mitochondrial activity independent of the number of attached cells. In this way, any direct biomaterial-dependent impact on mitochondrial activity could be analyzed. As shown in Figure 1C, total DNA quantification generally revealed a continuous increase in cell numbers until day 14 on all of the implant materials under study. Comparing individual biomaterials, our data further showed that at early culture periods, as indicated by days 1 and 3, cell number was elevated on titanium compared to the matched zirconia surfaces, while from day 7 onward, DNA quantity was comparable, irrespective of the biomaterial and on all surfaces (see also Table S2 in the Supporting Information). Since previous studies reported improved cell adhesion on rougher implant surfaces,[14,19] the increased DNA quantity on titanium at early culture time points in the present work may be due to improved initial cell adhesion compared to the moderately rough zirconia materials. Regarding AB reduction, however, osteoblasts on titanium displayed the lowest mitochondrial activity throughout the whole culture period, although they showed a similar trend as compared to 3Y-TZP and ZA_8Sr_8-Ce11 (Figure 1C and Table S2 (Supporting Information)). In this context, it was striking that mitochondrial activity had slightly decreased on 3Y-TZP and Ti at day 3 and peaked at day 7 on 3Y-TZP, ZA_8Sr_8-Ce11, and Ti, before declining again at day 14. By contrast, mitochondrial AB reduction on porous ZA_8Sr_8-$Ce11_p$ remained virtually unchanged until day 7 and decreased at day 14 to a degree to that seen with the previously mentioned surfaces. The decline in AB reduction at day 14 could be explained by a general decrease in mitochondrial activity caused by contact inhibition when reaching high cell density on the substratum, as quiescent cells have lower requirements for protein and nucleotide synthesis than do proliferating cells.[21] This suggestion is substantiated by the previous work of Leontieva and Blagosklonny, which demonstrated that contact inhibition in high density cell cultures is associated with deactivation of the mammalian target of rapamycin (mTOR) pathway.[22] In this context, mTOR acts as a major regulator of protein synthesis, mitochondrial energy, and cell proliferation by stimulating mitochondrial functions and biogenesis. By contrast, the slight decline in mitochondrial activity at day 3 and the subsequent increase at day 7 on 3Y-TZP and Ti seemed rather to be the result of time-dependent modulation in cell metabolism during the cell proliferation phase. Since there is to the best of our knowledge very little information to date on such time- and biomaterial-dependent modulation of mitochondrial activity, especially in the case of Ti which yielded the lowest AB reduction, the mechanism of this phenomenon remains to be established.

A possible link between implant surface properties and mitochondrial activity may be signaling pathways such as the phosphatidylinositol 3-kinase/Akt pathway which mediates cell–matrix/substrate signaling via integrin receptors,[23] and has been suggested to be involved in the regulation of mitochondrial activity by translocation of activated Akt into the mitochondrial matrix.[24] Therefore, our previous experiments revealed that cell functions, including morphogenesis, early cell adhesion, proliferation, and mitochondrial activity were modulated in both a time- and biomaterial-dependent manner. To test for putative effects on long-term cell attachment and osteogenic extracellular matrix (ECM) mineralization by the different biomaterial surfaces under study, we performed long-term cell culture experiments with osteoblasts over a period of 28 d. During this time, cells were cultured in growth medium (GM) and osteogenic culture medium to support ECM mineralization. To visualize the attached cells under growth conditions, the cells were stained with Azur II dye, whereas calcium deposition into the ECM during the mineralization process was examined by Alizarin Red S (ARS) staining.

Figure 2D summarizes the results of the Azur II and ARS staining after 28 d of culture on zirconia- and titanium-based disks. As can be seen from the Azur II staining, all biomaterials were completely covered with a confluent cell monolayer, distinguishable by a blue coloring, and demonstrating excellent long-term cell attachment on all of the surfaces examined. Regarding calcium deposition, however, ARS staining yielded differential coverage of the biomaterials with mineralized ECM, thereby strongly suggesting dependence of ECM formation and/or attachment on surface topography. On smoother surfaces, namely 3Y-TZP and partly ZA_8Sr_8-Ce11, ECM coverage was virtually absent, with few exceptions on ZA_8Sr_8-Ce11, whereas the rougher ZA_8Sr_8-$Ce11_p$ and Ti surfaces were completely covered with mineralized ECM, as indicated by the red stained areas. Additional staining of 3Y-TZP and ZA_8Sr_8-Ce11 disks with Azur II (data not shown) showed furthermore that the white unstained disk areas were not only free of mineralized ECM, but also lacking in attached cells. Since cell proliferation

and attachment under growth conditions was detectable on all biomaterials, it can be speculated that the presence of such cell/ECM-free areas on the smoother surfaces may be due to a poor long-term cell and/or ECM adhesion under osteogenic culture conditions. The main difference between the mineralized and nonmineralized osteoblast cultures was primarily in the deposition of calcium into the premature ECM, which most likely altered the mechanical properties of the matrix, making it more rigid than nonmineralized ECM and by this presumably more susceptible to mechanical stress-induced detachment caused by slight agitation possibly occurring during the long-term culture. Our data therefore indicate that the formation and/or long-term adhesion strength of mineralized bone-like matrix on the biomaterials' surface, which represents a prerequisite for successful hard tissue integration of implants,[25] was strongly affected by the surface topography and was obviously favored on biomaterials featuring more pronounced surface structures and increased area ratio (S_{dr}), namely ZA_8Sr_8-$Ce11_p$ and Ti, as compared to 3Y-TZP and ZA_8Sr_8-Ce11 (see also Table 1 for detailed IFM values). These results clearly point out the high impact of surface topography on mineralized ECM formation and/or attachment to biomaterials. Since due to the manufacturing process of the miniature implants for the animal study moderate changes in surface topography emerged which led to higher surface roughness of the zirconia-based surfaces as compared to the flat disks (Table 1), we also examined the formation and/or long-term adhesion of mineralized ECM on the 3D implant surfaces in vitro to check if cell behavior on the modified surfaces still correlated with previous results obtained from 2D disk cell cultures. When comparing 2D disk cell cultures (Figure 2D) with 3D miniture implant cultures (Figure 2E), it is evident that higher implant surface roughness (reflected by higher S_a, S_q, and S_{dr} values of the implants vs disks; Table 1) resulted in a considerable improvement in long-term cell and/or ECM adhesion on Impl.3Y-TZP and Impl.ZA_8Sr_8-Ce11, and to a lesser extent on Impl.ZA_8Sr_8-$Ce11_p$, which already showed good cell and ECM adhesion in 2D culture. Regarding the Ti-based miniture implants, surface treatment not only yielded lower surface roughness parameters than for Ti-based disks, but also surface properties more comparable to Impl.ZA_8Sr_8-$Ce11_p$, as reflected by similar S_a and S_q values (Table 1). Accordingly, the cell and/or ECM adhesion on Impl.Ti was as good as that on Impl.ZA_8Sr_8-$Ce11_p$ (Figure 1E). Hence, the trend toward improved bone-like ECM formation and/or adhesion with increasing surface roughness (S_a and S_q) and area ratio (S_{dr}) could be confirmed by the results from the 2D disk and 3D mini-implant long-term cultures. In summary, the results from the cell culture evaluation revealed that cell morphogenesis and metabolism, the latter reflected by mitochondrial activity, were considerably modulated in time- and biomaterial-dependent manner, demonstrating the weakest performance on Ti disks, which showed the roughest surface properties among the tested biomaterials. Furthermore, long-term cell attachment differed distinctly between culture modes, namely basal growth and osteogenic differentiation conditions. While under growth conditions, osteoblasts formed confluent monolayers on all biomaterial surfaces, cell and mineralized ECM attachment under osteogenic culture conditions were favored on rough and highly structured surfaces, namely ZA_8Sr_8-$Ce11_p$ and Ti.

2.3. Animal Study

Our previous cell culture experiments showed that the topographical properties of the biomaterials under study significantly affected cell morphogenesis, mitochondrial activity, and long-term attachment of mineralized bone-like ECM. At the tissue level, it is well known that the topographical and physicochemical surface properties of biomaterials play a crucial role for tissue integration during implant healing (reviewed in ref. [26]). Therefore, we became interested in the in vivo performance of the novel ceria-stabilized zirconia composite ZA_8Sr_8-Ce11 and the corresponding control materials, namely 3Y-TZP and Ti. To evaluate the implant healing into bone tissue after 14 and 28 d, we used the osseointegration research model established by Ogawa et al. which includes histomorphometrical analysis of the bone-to-implant-contact (BIC) and a biomechanical implant stability test, the so-called push-in test, in an established rat-animal model.[27] Within this study, 128 miniature implants were placed in the femurs of 64 rats for the histological analysis and biomechanical stability test, respectively.

All animals recovered well from the surgical intervention. Healing after surgery was uneventful for all but 7 animals, where wound dehiscences of the skin occurred after 1 d in one leg each. All dehiscences were immediately resutured. No further problems were observed. After a 28 d healing period, all histological sections showed areas where mineralized bone and bone marrow spaces contacted the implant surface (**Figure 3**). The histomorphometrical analysis revealed that the bone-to-implant contact after 14 d of healing in the cortical bone area was 28.1% for Impl.3Y-TZP, 24.9% for Impl.ZA_8Sr_8-Ce11, 72.6% for Impl.ZA_8Sr_8-$Ce11_p$, and 10.7% for Impl.Ti (**Table 2**). After 28 d healing, the respective BIC values in the cortical bone were 55.3% for Impl.3Y-TZP, 43.3% for Impl.ZA_8Sr_8-$Ce11_{os}$, 93.5% for Impl.ZA_8Sr_8-$Ce11_p$, and 16.9% for Impl.Ti. Accordingly, the porous Impl.ZA_8Sr_8-$Ce11_p$ surface showed the highest BIC values after 14 and 28 d, whereas the lowest values were seen with the Impl.Ti surface. For Impl.3Y-TZP and Impl.ZA_8Sr_8-Ce11 on the other hand, similar trends in BIC were observable at both time points, yielding significantly higher values than seen with Impl.Ti.

Regarding implant healing in the spongious bone areas, BIC values at day 14 amounted to 29.5% for Impl.3Y-TZP, 20.3% for Impl.ZA_8Sr_8-Ce11, 46.2% for Impl.ZA_8Sr_8-$Ce11_p$, and 25.1% for Impl.Ti. After 28 d of healing, the values for the zirconia materials almost doubled, whereas the BIC for Impl.Ti remained unchanged (Impl.3Y-TZP: 42%, Impl.ZA_8Sr_8-Ce11: 47.8%, Impl.ZA_8Sr_8-$Ce11_p$: 81.1%, Impl.Ti: 25.4%; Table 2). As already demonstrated for cortical bone healing, Impl.ZA_8Sr_8-$Ce11_p$ yielded here again the highest BIC values among all the tested implant surfaces at both times of examination, therefore pointing to a preference bone formation along the implant surface by the porous surface topography. With respect to the BIC after 28 d for the porous zirconia surface (Impl.ZA_8Sr_8-$Ce11_p$) used in this experiment, the values obtained are extraordinarily encouraging in comparison to other zirconia- and titanium-based implant surfaces examined to date,[28] and this also coincides with the results from the cell culture evaluation.

The push-in test was performed at 14 and 28 d after healing and provides information on the degree of osseointegration

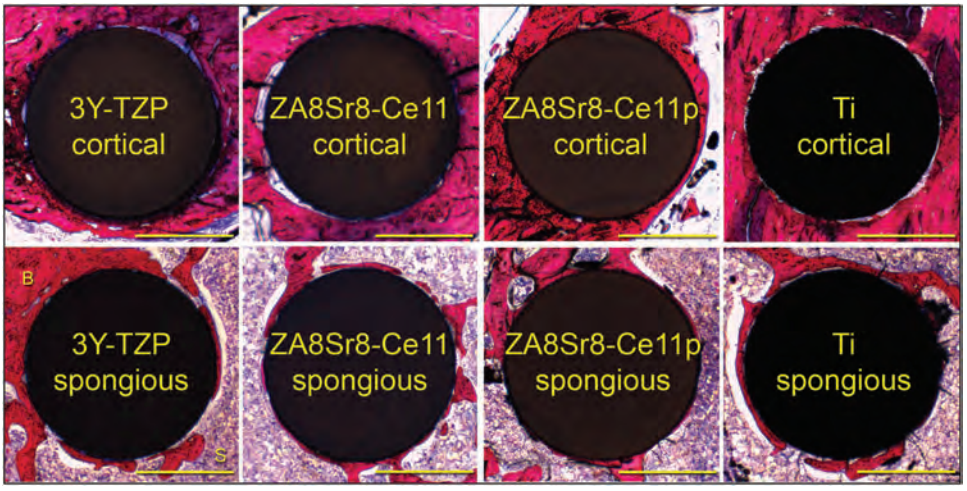

Figure 3. Histological specimens after 28 d of healing. The upper row shows the implants in the cortical bone area and the lower row the implants in the spongious bone area (scale bar: 500 µm). The red color indicates mineralized bone (B) and blue color indicates soft tissue (S). It is evident that all groups showed mineralized bone-to-implant, as well as soft tissue-to-implant contact.

by the breakpoint load at the implant–tissue interface. The average push-in values at 14 d were 10.2 N for Impl.3Y-TZP, 13.1 N for Impl.ZA_8Sr_8-Ce11, 63 N for Impl.ZA_8Sr_8-$Ce11_p$, and 23.9 N for Impl.Ti. Here, it is particularly noticeable that of all the implant groups, the porous Impl.ZA_8Sr_8-$Ce11_p$ surface showed by far the highest push-in value, whereas the moderately rough implants Impl.3Y-TZP and Impl.ZA_8Sr_8-Ce11 had similar values, and the rougher Impl.Ti surface was in between. This trend continued, in part, at day 28, thereby showing that the porous Impl.ZA_8Sr_8-$Ce11_p$ was again superior to the other implant surfaces. In detail, average push-in values at 28 d were 35.4 N for Impl.3Y-TZP, 31.5 N for Impl.ZA_8Sr_8-Ce11, 65.5 N for Impl.ZA_8Sr_8-$Ce11_p$, and 9.9 N for Impl.Ti (**Table 3**).

The time-dependent comparison between the push-in force at days 14 and 28 further revealed that the force values increased only for the moderately rough implant surfaces Impl.3Y-TZP and Impl.3Y-TZP, whereas in the Impl.ZA_8Sr_8-$Ce11_p$, no significant change in push-in force was detectable. This indicates that the maximum stability of the porous Impl.ZA_8Sr_8-$Ce11_p$ was achieved much more rapidly after only 14 d of healing and to a much larger extent since the push-in force remained two times higher at 28 d. These findings together with the results from the histomorphometric analysis add to the body of evidence that porous implant surfaces/coatings may give rise to improved implant fixation, which is thought to be a result of bone ingrowth into the pores.[29] Regarding the Impl.Ti control surfaces, this test group showed the poorest performance with respect to BIC and implant stability (push-in force), even with a deterioration of the results over time.

Table 2. Average bone-to-implant contact values of the examined surfaces in cortical and spongious bone areas at days 14 and 28 (mean values ± S.D.; $n = 8$ per group and healing period). The same superscript letter a, b, c indicates no significant difference between the groups (linear mixed model followed by Scheffe's post hoc test).

	Cortical bone-implant contact [%] ± S.D.			Spongious bone-implant contact [%] ± S.D.		
	14 d	28 d	*p*	14 d	28 d	*p*
Impl. 3Y-TZP	28.1 ± 16.1^{a}	55.3 ± 15.1^{b}	0.0036	29.5 ± 13.7^{a}	$42.0 \pm 17.8^{a,b}$	0.1386
Impl.ZA_8Sr_8-Ce11	24.9 ± 11.2^{a}	43.3 ± 16.9^{b}	0.0219	20.3 ± 15.1^{a}	47.8 ± 14.6^{b}	0.0024
Impl.ZA_8Sr_8-$Ce11_p$	72.6 ± 16.9^{b}	93.5 ± 7.2^{c}	0.0061	46.2 ± 16.6^{b}	81.1 ± 13.0^{c}	0.0004
Imp.Ti	10.7 ± 8.0^{a}	16.9 ± 6.4^{a}	0.1211	25.1 ± 9.5^{a}	25.4 ± 11.8^{a}	0.9612
p	<0.0001	<0.0001	–	0.0006	<0.0001	–

2.4. Microbiological Evaluation

The results from the cell-based in vitro evaluation and the animal study identified the novel porous ZA_8Sr_8-$Ce11_p$ surface to be the most promising dental implant biomaterial which promotes bone tissue integration. Another important issue in oral implant development is the avoidance of the formation of microbial biofilms, which can induce persistent biofilm-related infections such as peri-implantitis[17] and lead to inflammation driven bone resorption and finally even implant loss.[30] In this context, Albouy et al. demonstrated in a dog model that progression of experimentally induced peri-implantitis accompanied by plaque formation as well as the outcome of its treatment, including biofilm removal, are influenced by the implant surface characteristics.[31] Against this background, we examined the initial adhesion and oral biofilm formation of bacteria derived from human saliva on the porous ZA_8Sr_8-$Ce11_p$. Since it is well established that smooth surfaces with an as-pressed surface roughness (R_a) threshold of 0.2 µm impede unwanted biofilm formation and are therefore clinically established for the transcutaneous part of the implant, i.e., abutment,[32] we used a smooth ZA_8Sr_8-$Ce11_{ab}$ surface (ab = abutment; $R_a = 0.2$ µm, $S_a = 0.002$ µm, $S_q = 0.007$ µm, $S_{dr} = 0.002\%$, $S_{ds} = 7057$) as a control group to evaluate the microbiological performance of the porous ZA_8Sr_8-$Ce11_p$ surface.

In order to analyze initial adhesion and biofilm formation on ZA_8Sr_8-$Ce11_p$ and ZA_8Sr_8-$Ce11_{ab}$, we performed a quantitative

Table 3. Average push-in force to break the bone-to-implant contact at days 14 and 28 (mean values ± S.D.; $n = 8$ per group and healing period). The same superscript letter a, b indicates no significant difference between the groups in a column, i.e., between the different materials. The same superscript number 1, 2 indicates no significant difference between the different time points in a row, i.e., between 14 and 28 d of healing groups (linear mixed model followed by Scheffe's post hoc test).

	Push-in force to break the bone-to-implant contact [N] ± S.D.		
	14 d	28 d	*p*
Impl. 3Y-TZP	$10.2 \pm 6.6^{a,1}$	$35.4 \pm 20.7^{a,2}$	0.0055
Impl.ZA_8Sr_8-Ce11	$13.1 \pm 11.3^{a,1}$	$31.5 \pm 22.8^{a,2}$	0.0348
Impl.ZA_8Sr_8-$Ce11_p$	$63 \pm 25.2^{b,1}$	$65.5 \pm 23.7^{b,1}$	0.8424
Imp.Ti	$23.9 \pm 14.5^{b,1}$	9.9 ± 9.0^{1}	0.360
p	<0.0001	<0.0001	–

analysis of adherent microorganisms on the test surfaces at 2 h and 3 d post adhesion by determining the colony forming units (CFUs) after desorption of the adherent microorganisms by ultrasonication.[33] The CFUs derived from bacteria adherent to ZA_8Sr_8-$Ce11_p$ and the ZA_8Sr_8-$Ce11_{ab}$ control are illustrated in **Figure 4**A,B. Despite the different surface topographies, the experimental zirconia surfaces ZA_8Sr_8-$Ce11_p$ and ZA_8Sr_8-$Ce11_{ab}$ presented no significant differences in the bacterial growth of aerobic and anaerobic cultivable microorganisms after 2 h (initial adhesion) and 3 d (biofilm), respectively. Bacterial adhesion has been related to diverse surface parameters in the literature.[34] Among those parameters, average surface roughness has been the most studied[35] with regard to the antiadhesive behavior of numerous substrata.[36] As mentioned above, R_a values under 0.2 µm allow for the minimization of bacterial adhesion.[32] The more irregular and rougher an implant surface is, the more bacteria colonize the pores or grooves at the surface attachment sites of an implant[33] to a maximum interface contact in order to avoid desorption and shear stress.[37] Interestingly, in this report, surface roughness does not seem to correlate with initial bacterial adhesion or oral biofilm formation, as both surfaces presented comparable colonization rates of adherent bacteria. Another important parameter influencing bacterial adhesion on biomaterials is the chemical surface composition which exerts its impact via physiochemical surface properties, namely material hydrophobicity and charge.[38] In this context, it has been shown that biomaterials with similar physicochemical properties resulted in similar protein binding patterns and, therefore, the composition of salivary pellicle proteins.[39] Since in the present study both test biomaterials had the same surface chemistry, it can be speculated that the comparable bacterial colonization rates seen among the tested zirconia surfaces correlate with their similar physicochemical features and the electrophoretic attributes of salivary proteins following saliva coating. Our results therefore imply that the chemical composition rather than the porous surface structure of the new zirconia composite determined bacterial adhesion and biofilm formation, when compared to the smooth control surface.

Regarding the live/dead ratio of the attached bacteria to the porous ZA_8Sr_8-$Ce11_p$ and smooth ZA_8Sr_8-$Ce11_{ab}$ at 2 h and 3 d post adhesion, our data again found no significant difference in bacterial vitality between the two surfaces (Figure 4C,D). The percentage of live and/or metabolically active bacteria (green fluorescence) was thereby higher in the initial stage after 2 h (ZA_8Sr_8-$Ce11_p$: 68.46%; ZA_8Sr_8-$Ce11_{ab}$: 62.66%) than in the formed biofilm at day 3 (ZA_8Sr_8-$Ce11_p$: 11.15%; ZA_8Sr_8-$Ce11_{ab}$: 8.08%). Such a decline in bacterial vitality and/or metabolism may be part of the physiological process during biofilm formation, as in vivo data from Bürgers et al. revealed a high percentage of propidium iodide-positive bacteria in attached biofilms on titanium surfaces after only 12 h of intraoral incubation.[40] Since to our best knowledge, there is little information on saliva-derived oral biofilm formation and vitality on implant surfaces in vitro, our data emphasize the need for further studies on oral biofilm development on implant materials.

In summary, our results reveal no favoritism of biofilm formation by the rough ZA_8Sr_8-$Ce11_p$ when compared to the smooth control surface and points to a good microbiological performance in vivo and its potential as prospective oral implant biomaterial.

3. Conclusion

Since preclinical evaluation of newly developed medical devices in vitro and in vivo is a major issue for device success, we focused in this study on a three-pronged strategy, including the analysis with i) human osteoblasts on the cellular/molecular level, ii) an animal study focusing on the level of bone to implant contact, and iii) a microbiological assessment in terms of initial bacterial adhesion and biofilm formation. Within the LONGLIFE European project, we designed and developed innovative zirconia-based composites, in which equiaxial α-Al_2O_3 and elongated $SrAl_{12}O_{19}$ phases are dispersed in a ceria-stabilized zirconia matrix and commercial zirconia powders are coated by inorganic precursors of the second phases, which crystallize on the zirconia particles surface under proper thermal treatment. Interestingly, the preclinical evaluation data revealed the ceria-stabilized zirconia-based implant material ZA_8Sr_8-Ce11 in conjunction with a porous surface topography to be a superior material for clinical application and substantiated the transferability of this study to the in vivo situation by using human and tissue-specific cells as an in vitro screening element.

4. Experimental Section

Preparation of the Ceramic Specimens and Reference Materials: The synthesis of the new ceria-stabilized zirconia (Ce-TZP)-based composite was described in details elsewhere.[7] This composite, referred to as ZA_8Sr_8-Ce11, had the following composition: 84 vol% ZrO_2 – 8 vol% Al_2O_3 – 8 vol% $SrAl_{12}O_{19}$, in which ZrO_2 was stabilized by 11 mol% CeO_2. To process the composite, a commercial 10 mol% ceria-stabilized zirconia powder (Daiichi Kigenso Kagaku Kogio Co. Ltd., Japan) was dispersed in distilled water and aluminum, strontium, and ammonium cerium nitrates (Sigma-Aldrich) were added as precursors of α-alumina, strontium hexa-aluminate and to precisely tune the ceria content in the zirconia phase. The suspension was then spray-dried and thermally treated up to 1150 °C to obtain a triphasic zirconia–alumina–strontium aluminate powder. A 3Y-TZP (Tosoh TZY-E, Japan) powder was used as a benchmark powder.

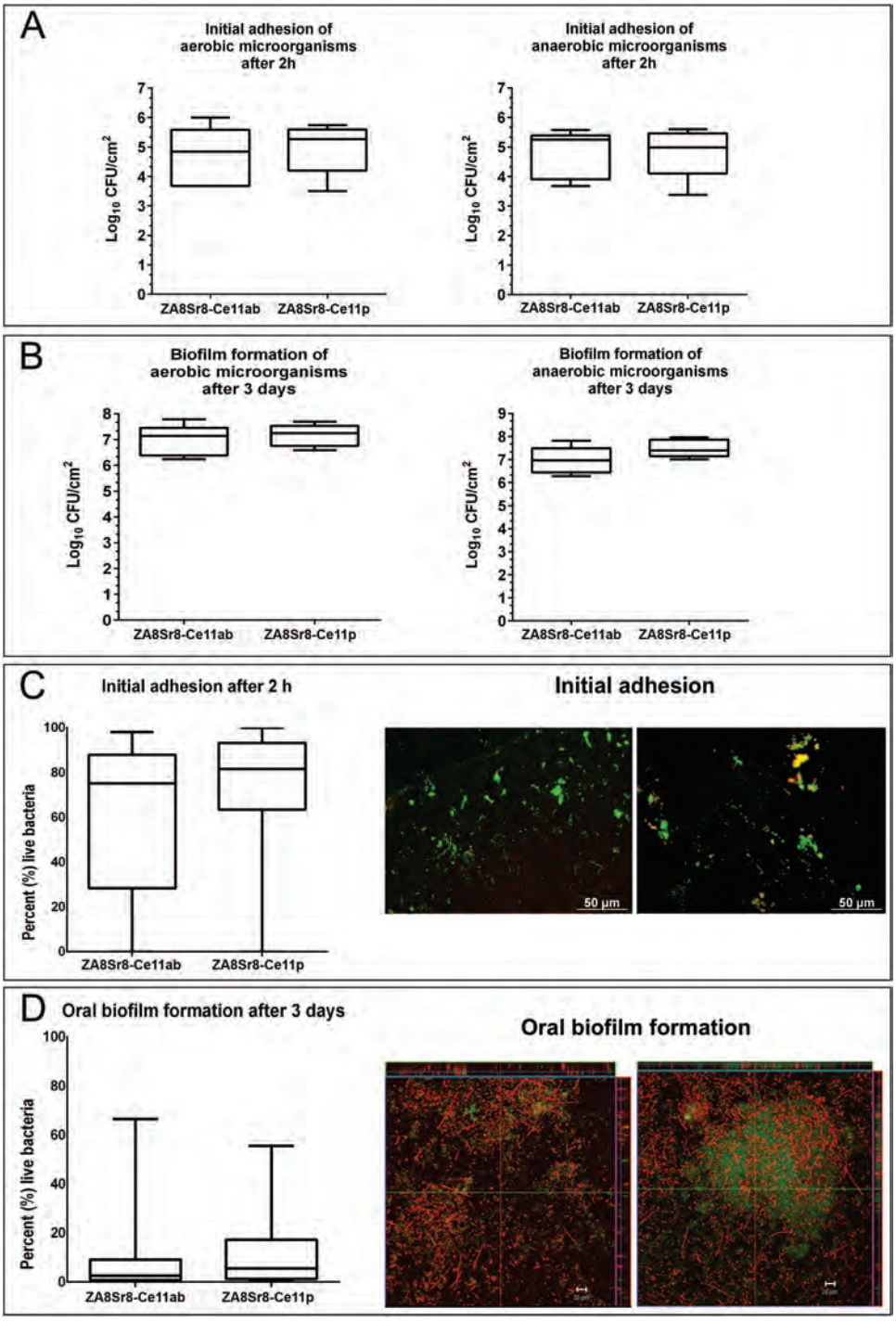

Figure 4. A,C) Initial bacterial adhesion of aerobic microorganisms after 2 h and B,D) biofilm formation after 3 d.

In order to compare the ZA_8Sr_8-Ce11 with conventional 3Y-TZP (control group) while retaining the same topography, a coating of both materials was applied by the same procedure on presintered substrates of 3Y-TZP. The coatings were applied by spraying a colloidal suspension of the respective powders. The suspensions were prepared by ball milling of the ceramic powders using zirconia milling media, a polyacrylic acid as the dispersant, and polyethylene glycol as the binder. As the coating was applied to presintered substrates, the homogeneous shrinkage allowed both to become densified at the same time and tightly linked. The thickness of the dense coating was a few micrometers. For ZA_8Sr_8-Ce11 with a porous surface structure (ZA_8Sr_8-Ce11$_p$), the Ce-TZP-based composite powder was applied on already sintered substrates of 3Y-TZP. When the coating was densified, shrinkage was only allowed in one direction due to the already dense substrate, contributing to an increased porosity of the coating. In addition to using 3Y-TZP as a reference ceramic material, titanium (Ti) was used as a "state-of-the-art" implant material in a further control group. The Ti-based specimens were made from titanium medical grade 23 (Ti-6Al-4V ELI) and

were sandblasted using air-borne particle abrasion with BCP (Anthogyr, Sallanches, France). For the microbiological evaluation, smooth ZA_8Sr_8-$Ce11_{ab}$ disks with surface properties representing an implant abutment area were prepared by leaving them with the as-pressed surface roughness of R_a = 0.2 µm. Biomaterial disks and implants destined for the biological evaluation were sterilized by low temperature hydrogen peroxide gas plasma sterilization STERRAD 100/100S (Advanced Sterilization Products [A.S.P], Johnson & Johnson Medical, Irvine, CA).

Surface Characterization: The surface topography of the specimen was analyzed by SEM (LEO435VP scanning electron microscope, Zeiss, Oberkochen, Germany) with the backscattered electron imaging mode and an accelerated voltage of 8.00–12.00 kV and light interferometry (MicroXAM 100 HR; ADE Phase Shift Technology). IFM measurements were made at three different areas on the specimen. To characterize the surface in height, spatial and surface enlargement, four parameters were selected: the main roughness parameters S_a and S_q describe the arithmetic mean (S_a) and the root-mean-square (S_q) values of the absolute surface asperity departures, S_{dr} describes the surface enlargement compared to a totally flat reference area in % or as a ratio, and S_{ds} measures the density of summits, i.e., number of peaks per area. Before parameter calculation, a digital (Gaussian) filter of 50 × 50 µm was applied in order to remove errors of form and waviness. The specimens used for SEM were sputter coated with gold–palladium for 60 s at 60 mA (SCD050; Balzers, Liechtenstein).

Culture of Primary Osteoblasts: Primary human osteoblasts were prepared from alveolar bone explants obtained from a 42 year old healthy male patient during an implant site preparation procedure. The collection of oral bone samples was approved by the Ethics Committee of the Albert Ludwigs University, Freiburg, Germany (vote Nr. 411/08_121010). Primary human alveolar bone osteoblasts were cultured in GM consisting of Dulbecco's modified Eagle's medium (PAA Laboratories, Coelbe, Germany) supplemented with 2% (w/v) glutamine (Gibco, Invitrogen, Karlsruhe, Germany), 10% (w/v) fetal calf serum (Biochrom AG, Berlin, Germany), and 0.2% (w/v) (50 µg mL^{-1}) kanamycin (Sigma-Aldrich, Taufkirchen, Germany). The cells were maintained in a humidified 37 °C incubator with 5% CO_2. All experiments were carried out with osteoblasts of passage 6. Extracellular matrix mineralization was induced by incubating confluent cultures with osteogenic medium consisting of growth medium supplemented with 10×10^{-3} M β-glycerophosphate disodium salt hydrate (Sigma-Aldrich), and 50 µg mL^{-1} sodium L-ascorbate (Sigma-Aldrich) for 28 d. For osteoblast culture on zirconia and titanium disks (15 mm diameter and 1 mm height) 0.5×10^4 cells mL^{-1} were seeded per disk in a 24-well plate (0.26×10^4 cm^{-2}).

Evaluation of Osteoblast Morphogenesis: Cell morphology of osteoblasts on the biomaterials under study was examined by SEM (LEO435VP) and fluorescence-based phalloidin-labeling of actin. Therefore, the cells were fixed with 4% formaldehyde in phosphate-buffered saline (PBS, Gibco) for 20 min at room temperature after 1 and 7 d of culture. For SEM analysis, specimens were then dehydrated in an ascending ethanol series (ranging from 30% to 100% ethanol (Sigma-Aldrich), three times each for 20 min at room temperature), critical point dried (CPD030 Critical Point Dryer; Bal-Tec AG, Balzers, Liechtenstein), and immediately sputter coated with gold–palladium for 60 s at 60 mA (SCD050; Balzers, Liechtenstein).

For actin staining, the samples were treated with 2% (w/v) bovine serum albumin (BSA, Sigma-Aldrich) and 0.2% TritonX-100 (Sigma-Aldrich) in PBS for 15 min at room temperature, and 2% (w/v) bovine serum albumin in PBS for a further 15 min at room temperature. The phalloidin conjugate was diluted in PBS containing 0.5% (w/v) BSA and samples were incubated for 30 min at room temperature with the diluted conjugate. Nuclei were stained with Hoechst 33258 (Sigma-Aldrich) for 5 min at room temperature. Optical evaluation was performed with a Biozero BZ-8000 fluorescence microscope (KEYENCE, Neu-Isenburg, Germany). Quantitative morphometric analysis was performed with the microscope software BZ Analyzer II from KEYENCE. To achieve statistically valid data, 2 to 4 disks per material group obtained from independent experiments and three areas per disk were analyzed. This resulted in a total number of 205–598 measured cells per material group and time point. Cell morphology parameters were the morphology index, which is the ratio between the long cell axis and short cell axis, describing the cell shape, and the cell area, which in turn provides information about the extent of cell spreading.

Evaluation of Cell Proliferation and Metabolic Activity: Metabolic activity of osteoblasts on zirconia- and titanium-based surfaces was assessed by the alamarBlue assay (AbD Serotec, Düsseldorf, Germany). The alamarBlue (AB) reagent comprises the redox-sensitive reporter dye resazurin, which is taken up by the cells and is reduced by mitochondrial respiration. The reduced product resorufin could be quantified in the supernatant by fluorometry. For this purpose, culture medium was replaced after 1, 3, 7, and 14 d of culture with medium containing 10% (w/v) AB reagent. After incubation for 3 h at 37 °C, samples of the supernatant were analyzed by measuring fluorescence (Tecan, Männedorf, Germany) according to the manufacturer's instructions. The percentage of AB reduction in the samples was calculated using a 100% reduced AB control as a reference, which was produced according to the manufacturer's protocol by autoclaving a sample containing culture medium with 10% (w/v) AB reagent for 15 min.

Cell density was examined by determining the DNA content on the zirconia and titanium disks after 1, 3, 7, and 14 d of culture. For this, specimens previously used for the AB assay were washed once with PBS after AB sampling, and lysed by a freeze-thaw cycle at –80 °C in 250 µL TE-buffer (10×10^{-3} M Tris-HCl, 1×10^{-3} M ethylenediaminetetraacetic acid (EDTA), pH 7.5). DNA quantification was performed with the Quant-iT PicoGreen assay (Invitrogen, Karlsruhe, Germany) according to the manufacturer's instructions.

Azur II and Alizarin Red S Staining: Long-term cell attachment to zirconia and titanium disks was visualized by Azur II staining after 28 d. Azur II is a cationic dye which stains basophilic cell structures and was used for unspecific staining of adherent cell monolayers. Calcium deposition into the ECM during the mineralization process by osteoblasts was analyzed by ARS staining at day 28. For both staining methods, cell layers attached to the disks were fixed in ice cold ethanol for 20 min, rinsed twice with distilled water, and stained for 30 min with 0.1% Azur II or 40×10^{-3} M ARS (Sigma-Aldrich).

Placements of Miniature Implants in the Rat Femur: The study protocol was approved by the Animal Research Committee of the University of Freiburg (35-9185.81/G-14/12). All animals were handled according to the policies and principles established by the German Animal Protection Law ("Deutsches Tierschutzgesetz"). Sixty four eight week old male Sprague-Dawley rats were used in this investigation. The animals were initially anesthetized before the surgical intervention in a plastic container with an isoflurane–oxygen mixture (3 vol% isoflurane in 100% oxygen with a flow of 4 L min^{-1}). After a deep anesthesia was reached, the animals were taken out of the inhalation chamber, a plastic mask was placed over the rat's snout, and the isoflurane concentration was reduced to 1.5–2 vol% isoflurane in 100% oxygen and a flow of 0.5–1 L min^{-1}. The hind legs of the animals were disinfected with a povidone-iodine solution (Braunol, B. Braun Melsungen AG, Melsungen, Germany). Subsequently, legs were shaved and additionally disinfected. For access to the femur, an incision on the dorsal side of the femur was made through the skin and the muscles and a full-thickness flap was reflected to expose the distal femur. The periosteum was reflected using periosteal elevators. One cylindrical implant per femur was placed ≈7–8 mm from the distal edge of the femur. The implant site was prepared by sequential drilling using a 0.7 mm round bur under sterile saline irrigation. With an endodontic file, the osteotomy was enlarged to 0.9 mm. The implants were then placed into the osteotomy and carefully pushed into place until the end of the implant was aligned with the femoral bone surface. After the correct implant position was achieved, the tissues were sutured in layers using resorbable sutures (Vicryl, Ethicon GmbH, Norderstedt, Germany). At the end of the surgical intervention, the animals received a subcutaneous analgesic (buprenorphine, 0.1 mg kg^{-1} body weight, every 7–9 h for 2 d) and antibiotic (doxycycline, 100 mg kg^{-1} body weight, one application) treatment. The wounds of the animals were controlled on a

daily basis and any occurring problems were registered. In the case of suture dehiscences, a resuturing was performed.

Sixty-four implants in 32 rats were placed for histological analysis and 64 implants were placed in 32 rats for the biomechanical test using the push-in method. Thirty-two animals were sacrificed after a healing period of 14 d and 32 after a healing period of 28 d using a lethal dose of CO_2 inhalation. The implants of the Impl.Ti and Impl.ZA_8Sr_8-Ce11$_p$ group were placed into the left and right femurs, respectively, of the same rats, whereas the groups Impl.3Y-TZP and Impl.ZA_8Sr_8-Ce11 were placed in the femurs of other rats. The distribution of the implants can be seen in Table S3 (Supporting Information).

Histological Procedure and Histomorphometric Analysis: The femurs of the animals were dissected free and the soft tissue was removed using scalpels and periosteal elevators. After rinsing the harvested implant-femur specimens of the histological groups (with 14 and 28 d of healing) thoroughly with saline, they were immersed in 4% buffered formalin for two weeks at 4 °C. Then, the specimens were processed for histological evaluation according to the method of Donath and Breuner.[41] To remove the fixation solution, the specimens were rinsed in water. They were then dehydrated over a period of 18 d using an increasing alcohol gradient (50–100% ethanol, seven steps). The specimens were then embedded in Technovit 9100 (Heraeus Kulzer, Wehrheim, Germany). This is a polymerization system based on methyl methacrylate which hardens at low temperature. The chemical process takes place under the exclusion of oxygen with the aid of a catalyst composed of peroxide and an amine component. Additional components such as poly(methyl methacrylate) powder and a regulator allow controlled polymerization. First, the specimens were preinfiltrated under permanent agitation at room temperature and then infiltrated at 4 °C. Then, the samples that were positioned in containers and completely covered with polymerization mixture were placed into a freezer and left to polymerize at −18 °C for two weeks. The samples were stored afterward at 4–8 °C (refrigerator) for at least 1 h before being allowed to come slowly to room temperature. When the samples were brought to ambient temperature, they were cut, grinded, and glued (Technovit 7210 VLC, Heraeus Kulzer GmbH, Wehrheim, Germany) on object slides.

Following the preparation process, the specimens were prepared with the use of the cutting–grinding system (EXAKT-Apparatebau, Norderstedt, Germany) to get the final desired thickness. For the grinding process, sandpapers of decreasing grits were used, beginning with 800 grits and finishing with polishing grain size of 4000 grit. The final cut layer thickness was 60–80 µm and was digitally verified (Mikrometer AW-10, EXAKT Apparatebau). Finally, the specimens obtained were stained with Azur II and pararosaniline.[42]

The sections through the implants were performed in a horizontal direction: one section was performed in the cortical bone layer and one in the spongious bone layer. Accordingly, two histological sections could be obtained from each implant.

Histological observations and computer-assisted histomorphometric analysis were performed using a Zeiss Axioskop (Zeiss, Oberkochen, Germany) equipped with a video camera (ColorView III, Olympus, Münster, Germany) and the software program cell (Olympus, Münster, Germany). The histomorphometric analysis comprised the evaluation of the fraction of the implant in contact to the cortical and spongious bone, respectively, using different magnifications (10×, 20×, 40× magnification). The healing periods as well as the implant materials/surfaces were unknown to the interpreter (blinded interpretation).

Implant Push-In Test: After harvesting, the implant-femur specimens of groups C and D (Table S3, Supporting Information) were immediately embedded into an autopolymerizing resin (Technovit 4071, Heraeus Kulzer, Wehrheim, Germany) in a custom-made metal mold. The implants were subsequently loaded axially in a universal testing machine (Zwick, Ulm, Germany) with a 10 kN load cell and a 0.8-mm-diameter stainless steel pushing rod. The crosshead speed was 10 mm min^{-1}. The applied load and the displacement of the implant were monitored.

Culture of Salivary Bacteria: Paraffin-stimulated (CRT, Ivoclar Vivadent AG, Schaan, Liechtenstein) human saliva (50 mL per proband) was obtained from six healthy volunteers who refrained from antibiotic use within the last 30 d prior to the beginning of the study. The study protocol was approved by the Ethics Committee of the Albert Ludwigs University of Freiburg (Nr. 91/15). The saliva was stored at −80 °C prior to use, while after the bacterial adhesion tests, the adherent salivary bacteria were cultivated under both aerobic and anaerobic conditions on Columbia blood agar plates (CBA, Becton Dickinson, Heidelberg, Germany) at 37 °C and 5% CO_2 and in anaerobic jars (Anaerocult A; Merck, Darmstadt, Germany) on yeast–cysteine blood agar (HCB) plates overnight, respectively.[43] The optical density of the salivary suspensions was assessed at 595 nm (Bio-Rad, Life Science Group, Hercules, CA, USA) against 0.9% saline solution (NaCl) as a blank. The following assays were performed as multispecies experiments.

CFUs: Three samples of each material surface were placed into multiwell plates (12-well plate; Greiner Bio-One, Frickenhausen, Germany), one sample in each well. The samples were then stabilized by an A-silicone compound (Aquasil Ultra XLV; Dentsply, Milford, DE, USA) so that solely their upper surfaces remained uncovered by silicon, as described elsewhere.[44] Afterward, 2 mL of the salivary suspension was injected onto each sample surface and was under constant swirling at 37 °C (5% CO_2) for 2 h and 3 d, respectively. The silicone was then separated from the samples, which were washed twice with 5 mL 0.9% NaCl solution and nonadherent bacteria were removed from the margins by sterile foam pellets (Voco GmbH, Cuxhaven, Germany). Finally, the adherent microorganisms were dislodged from the sample surfaces after ultrasonication for 1 min in 1 mL 0.9% NaCl on ice and several dilutions thereof were plated onto the CBA or HCB agar plates for the determination of CFUs. This protocol was applied three times, obtaining an average of nine independent measurements for each material group.

Live/Dead Staining: The visualization of both live and dead adherent bacteria was aided by SYTO 9 dye and propidium iodide (PI) (Live/Dead BacLight Bacterial Viability Kit, Life Technologies GmbH, Darmstadt, Germany) as described in a previous report.[45] In short, the fluorescent dye was diluted to a concentration of 2/20 nmol mL^{-1} by adding in 0.9% NaCl. Following incubation of the samples with salivary bacteria in a multiwell plate (12-well plate; Greiner Bio-One, Frickenhausen, Germany) at 37 °C for 2 h and 3 d (5% CO_2), respectively, 2 mL SYTO 9/PI in 0.9% NaCl was inserted into each well. After the 2 h incubation, the samples were stabilized with superglue (Loctite 401, Loctite Deutschland GmbH, Munich, Germany) onto a slide and stored for 10 min in a dark chamber. Representative images were acquired for illustration of the vitality rates. After the 3 d incubation, the samples positioned face down onto a drop of 0.9% NaCl chambered coverglass (μ Slide 8 well, ibidi GmbH, Munich, Germany) and monitored by confocal laser scanning microscopy (Leica TCS SP2 AOBS, Mannheim, Germany) with a 63× water immersion objective (HCX PL APO/bd. BL 63.0 × 1.2 W, Leica, Mannheim, Germany). The 3 d old biofilms were quantified by screening at three representative positions. The mean biofilm thickness was measured after establishing the upper and lower boundaries of the biofilms at these three points, which were then scanned in the *Z* direction. As a result, 0.5-µm-thick optical sections at 2 µm intervals were obtained throughout the biofilms. The 1.7 zoom setting corresponded to physical dimensions of 140 × 140 µm, and digital images of 1024 × 1024 pixels. Sequential scanning minimized the risk of spectral overlap. This assay was repeated twice, in duplicate.

Statistical Analysis: Data obtained by interferometry were analyzed using one-way ANOVA followed by Tukey's post hoc test. The cell culture experiments were performed in triplicate in three independent experiments (unless otherwise indicated). Differences between groups were examined for statistical significance using a one-way ANOVA followed by Tukey's post hoc test for normally distributed data and a Kruskal–Wallis ANOVA followed by Dunn's post hoc test for non-normally distributed data. For data obtained from the animal experiments, a linear mixed model was fitted with random intercepts for each animal to evaluate time and surface effects on the response variable. Animals were considered as clusters since data are collected with several surfaces per animal. Furthermore, pairwise comparisons were performed. For statistical evaluation of the microbiological data, a one-way ANOVA per response variable (aerobia, anaerobia) was applied

to check for differences among the two different implants. A linear mixed model was fitted with random intercepts to evaluate material effects on response variables (live/dead), while pairwise comparisons between the two implant groups were conducted. The method of "Scheffe" was applied to correct for the multiple testing problem (adjustment of *p* values). The calculations were performed with the statistical software STATA 13 (StataCorp LP, College Station, USA). The significance level was set at 5%.

Supporting Information

Supporting Information is available from the Wiley Online Library or from the author.

Acknowledgements

B.A. and L.K. contributed equally to this work, whereas T.S. and R.J.K. are co-senior authors of this paper. The authors express their gratitude to Anja Stork, Bettina Spitzmüller, and Yrgalem Abreha for their excellent technical help. Janna Bruns and Raimo Ewert are thanked for their valuable contribution to this report and support by image processing. The authors also thank Kirstin Vach for the comprehensive statistical evaluation of the data obtained from the animal experiments.

The research leading to these results was performed within the LONGLIFE project and received funding from the European Community's Seventh Framework Programme (FP7/2007–2013) under grant agreement no. 280741.

Conflict of Interest

The authors declare no conflict of interest.

Keywords

bacterial adhesion, human osteoblasts, implant materials, osseointegration, zirconia-based composites

Received: May 10, 2017
Revised: July 1, 2017
Published online:

[1] a) M. N. Aboushelib, E. Osman, I. Jansen, V. Everts, A. J. Feilzer, *J. Prosthodontics* **2013**, *22*, 190; b) M. Bächle, F. Butz, U. Hübner, E. Bakalinis, R. J. Kohal, *Clin. Oral Implants Res.* **2007**, *18*, 53; c) R. Depprich, M. Ommerborn, H. Zipprich, C. Naujoks, J. Handschel, H. P. Wiesmann, N. R. Kubler, U. Meyer, *Head Face Med.* **2008**, *4*, 29; d) S. H. Han, K. H. Kim, J. S. Han, K. T. Koo, T. I. Kim, Y. J. Seol, Y. M. Lee, Y. Ku, I. C. Rhyu, *J. Periodontal Implant Sci.* **2011**, *41*, 227; e) R. J. Kohal, M. Bächle, W. Att, S. Chaar, B. Altmann, A. Renz, F. Butz, *Dent. Mater.* **2013**, *29*, 763.

[2] a) M. N. Aboushelib, N. A. Salem, A. L. Taleb, N. M. El Moniem, *J. Oral Implantol.* **2013**, *39*, 583; b) Y. Akagawa, R. Hosokawa, Y. Sato, K. Kamayama, *J. Prosthet. Dent.* **1998**, *80*, 551; c) M. Gahlert, S. Roehling, C. M. Sprecher, H. Kniha, S. Milz, K. Bormann, *Clin. Oral Implants Res.* **2012**, *23*, 281.

[3] M. Andreiotelli, R. J. Kohal, *Clin. Implant Dent. Relat. Res.* **2009**, *11*, 158.

[4] a) N. R. Silva, P. G. Coelho, C. A. Fernandes, J. M. Navarro, R. A. Dias, V. P. Thompson, *J. Biomed. Mater. Res., Part B* **2009**, *88*, 419; b) N. R. Silva, P. Nourian, P. G. Coelho, E. D. Rekow, V. P. Thompson, *Clin. Implant Dent. Relat. Res.* **2011**, *13*, 168.

[5] J. Chevalier, L. Gremillard, A. V. Virkar, D. R. Clarke, *J. Am. Ceram. Soc.* **2009**, *92*, 1901.

[6] J. Chevalier, L. Gremillard, S. Deville, *Annu. Rev. Mater. Res.* **2007**, *37*, 1.

[7] P. Palmero, M. Fornabaio, L. Montanaro, H. Reveron, C. Esnouf, J. Chevalier, *Biomaterials* **2015**, *50*, 38.

[8] H. Reveron, M. Fornabaio, P. Palmero, T. Fürderer, E. Adolfsson, V. Lughi, A. Bonifacio, V. Sergo, L. Montanaro, J. Chevalier, *Acta Biomater.* **2017**, *48*, 423.

[9] L. Montanaro, P. Palmero, J. Chevalier, H. Reveron, T. Fürderer, Google Patents, US2017057876 (A1), EP3107861 (A1), **2016**.

[10] a) M. J. Kim, C. W. Kim, Y. J. Lim, S. J. Heo, *J. Biomed. Mater. Res., Part A* **2006**, *79*, 1023; b) H. Schweikl, R. Müller, C. Englert, K. A. Hiller, R. Kujat, M. Nerlich, G. Schmalz, *J. Mater. Sci.: Mater. Med.* **2007**, *18*, 1895; c) G. Wang, X. Liu, H. Zreiqat, C. Ding, *Colloids Surf., B* **2011**, *86*, 267.

[11] T. Sawase, R. Jimbo, K. Baba, Y. Shibata, T. Ikeda, M. Atsuta, *Clin. Oral Implants Res.* **2008**, *19*, 491.

[12] H. Aita, W. Att, T. Ueno, M. Yamada, N. Hori, F. Iwasa, N. Tsukimura, T. Ogawa, *Acta Biomater.* **2009**, *5*, 3247.

[13] W. Att, M. Takeuchi, T. Suzuki, K. Kubo, M. Anpo, T. Ogawa, *Biomaterials* **2009**, *30*, 1273.

[14] L. Zhao, S. Mei, P. K. Chu, Y. Zhang, Z. Wu, *Biomaterials* **2010**, *31*, 5072.

[15] a) B. Altmann, T. Steinberg, S. Giselbrecht, E. Gottwald, P. Tomakidi, M. Bachle-Haas, R. J. Kohal, *Biomaterials* **2011**, *32*, 8947; b) E. Gentleman, R. J. Swain, N. D. Evans, S. Boonrungsiman, G. Jell, M. D. Ball, T. A. Shean, M. L. Oyen, A. Porter, M. M. Stevens, *Nat. Mater.* **2009**, *8*, 763; c) C. H. Lohmann, L. F. Bonewald, M. A. Sisk, V. L. Sylvia, D. L. Cochran, D. D. Dean, B. D. Boyan, Z. Schwartz, *J. Bone Miner. Res.* **2000**, *15*, 1169; d) X. Rausch-fan, Z. Qu, M. Wieland, M. Matejka, A. Schedle, *Dent. Mater.* **2008**, *24*, 102; e) P. Torricelli, M. Fini, G. Giavaresi, R. Giardino, *Artif. Cells, Blood Substitutes, Immobilization Biotechnol.* **2003**, *31*, 263.

[16] D. Lebeaux, N. Fernandez-Hidalgo, A. Chauhan, S. Lee, J. M. Ghigo, B. Almirante, C. Beloin, *Lancet Infect. Dis.* **2014**, *14*, 146.

[17] A. Monje, L. Aranda, K. T. Diaz, M. A. Alarcon, R. A. Bagramian, H. L. Wang, A. Catena, *J. Dent. Res.* **2016**, *4*, 372.

[18] J. Lindhe, J. Meyle, *J. Clin. Periodontol.* **2008**, *35*, 282.

[19] B. Altmann, R. J. Kohal, T. Steinberg, P. Tomakidi, M. Bächle, A. Wennerberg, W. Att, *Tissue Eng., Part C* **2013**, *19*, 850.

[20] G. Passeri, A. Cacchioli, F. Ravanetti, C. Galli, E. Elezi, G. M. Macaluso, *Clin. Oral Implants Res.* **2010**, *21*, 756.

[21] M. Morita, S. P. Gravel, L. Hulea, O. Larsson, M. Pollak, J. St-Pierre, I. Topisirovic, *Cell Cycle* **2015**, *14*, 473.

[22] O. V. Leontieva, M. V. Blagosklonny, *Cell Cycle* **2014**, *13*, 509.

[23] P. J. Marie, E. Hay, Z. Saidak, *Trends Endocrinol. Metab.* **2014**, *25*, 567.

[24] H. M. McBride, M. Neuspiel, S. Wasiak, *Curr. Biol.* **2006**, *16*, R551.

[25] J. E. Davies, *J. Dent. Educ.* **2003**, *67*, 932.

[26] a) K. Anselme, A. Ponche, M. Bigerelle, *Proc. Inst. Mech. Eng., Part H* **2010**, *224*, 1487; b) R. A. Gittens, L. Scheideler, F. Rupp, S. L. Hyzy, J. Geis-Gerstorfer, Z. Schwartz, B. D. Boyan, *Acta Biomater.* **2014**, *10*, 2907; c) A. Wennerberg, T. Albrektsson, *Clin. Oral Implants Res.* **2009**, *20*, 172.

[27] T. Ogawa, S. Ozawa, J. H. Shih, K. H. Ryu, C. Sukotjo, J. M. Yang, I. Nishimura, *J. Dent. Res.* **2000**, *79*, 1857.

[28] a) R. J. Kohal, M. Bachle, A. Renz, F. Butz, *Dent. Mater.* **2016**, *32*, 65; b) G. Manzano, L. R. Herrero, J. Montero, *Int. J. Oral Maxillofac. Implants* **2014**, *29*, 311; c) N. R. Silva, I. Sailer, Y. Zhang, P. G. Coelho, P. C. Guess, A. Zembic, R. Kohal, *Materials* **2010**, *3*,

863; d) D. S. Thoma, G. I. Benic, F. Munoz, R. Kohal, I. Sanz Martin, A. G. Cantalapiedra, C. H. Hämmerle, R. E. Jung, *J. Clin. Periodontol.* **2015**, *42*, 967.
[29] a) A. Chaudhari, A. Braem, J. Vleugels, J. A. Martens, I. Naert, M. V. Cardoso, J. Duyck, *PLoS One* **2011**, *6*, e24186; b) G. Ryan, A. Pandit, D. P. Apatsidis, *Biomaterials* **2006**, *27*, 2651.
[30] E. Rompen, O. Domken, M. Degidi, A. E. Pontes, A. Piattelli, *Clin. Oral Implants Res.* **2006**, *17*, 55.
[31] a) J. P. Albouy, I. Abrahamsson, T. Berglundh, *J. Clin. Periodontol.* **2012**, *39*, 182; b) J. P. Albouy, I. Abrahamsson, L. G. Persson, T. Berglundh, *J. Clin. Periodontol.* **2011**, *38*, 58.
[32] W. Teughels, N. Van Assche, I. Sliepen, M. Quirynen, *Clin. Oral Implants Res.* **2006**, *17*, 68.
[33] A. Al-Ahmad, M. Wiedmann-Al-Ahmad, A. Fackler, M. Follo, E. Hellwig, M. Bächle, C. Hannig, J. S. Han, M. Wolkewitz, R. Kohal, *Arch. Oral Biol.* **2013**, *58*, 1139.
[34] R. J. Crawford, H. K. Webb, V. K. Truong, J. Hasan, E. P. Ivanova, *Adv. Colloid Interface Sci.* **2012**, *179*, 142.
[35] T. Shida, H. Koseki, I. Yoda, H. Horiuchi, H. Sakoda, M. Osaki, *Int. J. Nanomed.* **2013**, *8*, 3955.
[36] D. Siegismund, A. Undisz, S. Germerodt, S. Schuster, M. Rettenmayr, *Acta Biomater.* **2014**, *10*, 267.
[37] M. Katsikogianni, I. Spiliopoulou, D. P. Dowling, Y. F. Missirlis, *J. Mater. Sci.: Mater. Med.* **2006**, *17*, 679.
[38] M. Katsikogianni, Y. F. Missirlis, *Eur. Cells Mater.* **2004**, *8*, 37.
[39] a) M. Fukuta, N. Zettsu, I. Yamashita, Y. Uraoka, H. Watanabe, *Colloids Surf., B* **2013**, *102*, 435; b) E. M. Lima, H. Koo, A. M. Vacca Smith, P. L. Rosalen, A. A. Del Bel Cury, *Clin. Oral Implants Res.* **2008**, *19*, 780.
[40] R. Bürgers, T. Gerlach, S. Hahnel, F. Schwarz, G. Handel, M. Gosau, *Clin. Oral Implants Res.* **2010**, *21*, 156.
[41] K. Donath, G. Breuner, *J. Oral Pathol.* **1982**, *11*, 318.
[42] J. Laczko, G. Levai, *Mikroskopie* **1975**, *31*, 1
[43] C. Senges, K. T. Wrbas, M. Altenburger, M. Follo, B. Spitzmüller, A. Wittmer, E. Hellwig, A. Al-Ahmad, *J. Endod.* **2011**, *37*, 1247.
[44] S. Schienle, A. Al-Ahmad, R. J. Kohal, F. Bernsmann, E. Adolfsson, L. Montanaro, P. Palmero, T. Fürderer, J. Chevalier, E. Hellwig, L. Karygianni, *Clin. Oral Invest.* **2016**, *7*, 1719.
[45] P. N. Tawakoli, A. Al-Ahmad, W. Hoth-Hannig, M. Hannig, C. Hannig, *Clin. Oral Invest.* **2013**, *17*, 841.